Contents lists available at ScienceDirect

Bioactive Materials

C176-loaded and phosphatidylserine-modified nanoparticles treat retinal neovascularization by promoting M2 macrophage polarization

An Shao [a,†], Lulu Jin [b,†], Yanni Ge [a], Ziqiang Ye [b], Mingyu Xu [a], Yifan Zhou [a], Yingyu Li [a], Linyan Wang [a], Pinglong Xu [c], Kai Jin [a,***], Zhengwei Mao [b,**], Juan Ye [a,*,1]

[a] *Eye Center, The Second Affiliated Hospital, School of Medicine, Zhejiang University, Hangzhou, 310009, China*
[b] *MOE Key Laboratory of Macromolecular Synthesis and Functionalization, Department of Polymer Science and Engineering, Zhejiang University, Hangzhou, 310027, China*
[c] *MOE Key Laboratory of Biosystems Homeostasis & Protection and Zhejiang Provincial Key Laboratory of Cancer Molecular Cell Biology, Life Sciences Institute, Zhejiang University, Hangzhou, 310030, China*

A R T I C L E   I N F O

A B S T R A C T

Retinal neovascularization (RNV), a typical pathological manifestation involved in most neovascular diseases, causes retinal detachment, vision loss, and ultimately irreversible blindness. Repeated intravitreal injections of anti-VEGF drugs were developed against RNV, with limitations of incomplete responses and adverse effects. Therefore, a new treatment with a better curative effect and more prolonged dosage is demanding. Here, we induced macrophage polarization to anti-inflammatory M2 phenotype by inhibiting cGAS-STING signaling with an antagonist C176, appreciating the role of cGAS-STING signaling in the retina in pro-inflammatory M1 polarization. C176-loaded and phosphatidylserine-modified dendritic mesoporous silica nanoparticles were constructed and examined by a single intravitreal injection. The biosafe nanoparticles were phagocytosed by retinal macrophages through a phosphatidylserine-mediated "eat me" signal, which persistently release C176 to suppress STING signaling and thereby promote macrophage M2 polarization specifically. A single dosage can effectively alleviate pathological angiogenesis phenotypes in murine oxygen-induced retinopathy models. In conclusion, these C176-loaded nanoparticles with enhanced cell uptake and long-lasting STING inhibition effects might serve as a promising way for treating RNV.

1. Introduction

Retinal neovascularization (RNV) is the typical pathological manifestation in retinopathy of prematurity (ROP), proliferative diabetic retinopathy (PDR) and other retinal neovascular diseases. The diffused leaky neovascular tissues in the retina can protrude inwards to the vitreous cavity or extend outwards to the subretinal area, which consequently causes vitreous hemorrhage and exudative retinal detachment and finally leads to irreversible blindness in severe cases [1–3].

Recently, intravitreal drugs such as aflibercept were widely used for treating RNV due to their direct anti-vascular endothelial growth factor (VEGF) effect [4–10]. However, incomplete responses (e.g., suboptimal vision recovery) to anti-VEGF drugs represent significant clinical unmet needs [11,12]. Moreover, repeated and long-term intravitreal injections can increase the chance of ocular and systemic complications including intraocular inflammation and acute blood pressure elevations [13,14].

There is increasing evidence that the activated macrophages within/around the neovascular tissue are the major contributors to the

inflammatory microenvironment, leading to pathological angiogenesis [15–17]. The macrophages are highly plastic with diverse morphologies and functions. Based on the secreted cytokines, they can be roughly divided into M1 pro-inflammatory state and M2 anti-inflammatory state [18], which have been important targets for treating tumors and inflammatory diseases. Studies have reported that the macrophages are first polarized to the M1 state and then undergo M2 activation in the development of RNV. Nanoparticles (NPs) loaded with miRNA-233 showed a satisfactory therapeutic effect on ROP by promoting macrophages to the anti-inflammatory M2 state in the early stage [19,20]. Another study had reported that the M2 macrophages play an important role in promoting vascular remodeling in retinal neovascular diseases [21]. Thus, it is a promising way to treat retinal neovascular diseases by modulating the polarization of macrophages to the M2 subtype in the early pathological stage of RNV.

Recently, the cyclic GMP-AMP synthase (cGAS)-stimulator of interferon genes (STING) pathway has been found to be a highly versatile innate immune sensing system, which is dominantly activated in the myeloid cells, including macrophages, in the inflammatory niche compared to other cell types [22,23]. The specific processes are as follows: cellular stress-induced double-strand DNA binds to and activates cGAS to form cGAMP. cGAMP binds to STING on the endoplasmic reticulum membrane and translocates to the Golgi apparatus, where STING recruits TBK1 and IRF3. The phosphorylation of these messenger proteins finally induces the expression of various downstream inflammatory genes, causing the M1 polarization of macrophages. Meanwhile, the association between the inhibition of the cGAS-STING pathway and the M2 macrophage polarization remains further elucidation [24–27]. While inhibitors for STING are still in development, C176, a known and potent small-molecule inhibitor of STING, can effectively treat rheumatoid arthritis and ischemic stroke by attenuating inflammation [28, 29]. Given that the aberrant macrophage polarization is one of the initiators of pathological angiogenesis, we hypothesized that inhibiting the STING pathway via C176 can induce M2 polarization of macrophages and might serve as an alternative treatment for retinal neovascular diseases.

Intravitreal injection is the most direct way to deliver drugs to retinal tissue without crossing the blood-eye barrier and minimize the side effects of normal tissues as eyes are relatively isolated from blood circulation [30]. However, most of the previous studies focused on the systemic use of STING antagonist, and small molecule drugs such as C176 have poor tissue retention and, thus require frequent local injections [28,29], which seriously affect the adherence of patients to a large extent [31,32]. Besides, the hydrophobicity of C176 makes it easily agglomerate in the interstitial fluid, resulting in decreased efficacy [33, 34]. Moreover, although macrophages are a relatively small group of cells in retina, they are the major contributors of inflammation during RNV. Therefore, long-lasting dosage forms with specific cell delivery capabilities are urgently needed to be developed to improve the treatment. Fortunately, the emergence of drug carriers can solve these problems by improving the utilization and efficacy of drugs through sustained drug release, thus reducing the frequency of administration [35,36]. As a promising platform for drug delivery, silica nanoparticles have good biological properties including biocompatibility, biodegradability and slow-release properties, which have been approved by the Food and Drug Administration. However, the silica nanoparticles without pores or with relatively small pore size limited their drug-loading capacity. Therefore, dendritic mesoporous silica nanoparticles (DMSNs) with comparably increased pore sizes and porosity serve as a customized storage of drugs in this study. These DMSNs demonstrate high loading capacity of hydrophobic drugs, making them an ideal nanocarrier for the aggressive intravitreal delivery in ophthalmic medications [37–40]. Moreover, DMSNs have been reported to protect drugs from enzymatic degradation and exhibited enhanced cellular uptake properties, which helps improve drug efficacy. To further prolong the therapeutic drug levels on retinal macrophages, we encapsulated DMSNs into liposomes modified with phosphatidylserine (PS). Macrophages can recognize PS on the liposome membrane which acts as an "eat me" signal by promoting phagocytosis, and thereby achieving the selective drug delivery. Studies also have validated the positive correlation between the proportion of PS in the liposomes and the cell uptake [41-44].

Herein, DMSNs loaded with C176 were prepared and modified with liposomes containing PS (PS@DMSN-C176). PS@DMSN-C176 NPs were specially designed for the intravitreal administration of STING antagonist in treating RNV and the function was made up of 3 parts: (i) C176 attenuates the inflammation by inhibiting the cGAS-STING pathway and promoting the M2 polarization of macrophages; (ii) DMSNs can load drugs and release the drug slowly to prolong the therapeutic effects; (iii) PS-modified liposomes enhance their uptake by retinal macrophages (Scheme 1). After optimizing the encapsulation efficiency of C176 and the proportion of PS in liposomes, these PS@DMSN-C176 NPs were used to treat mice with oxygen-induced retinopathy (OIR). We evaluate their ability to attenuate inflammation by promoting M2 polarization and inhibiting cGAS-STING pathway, which achieves long-lasting and effective anti-inflammation during retinal pathological angiogenesis and showed satisfactory results via a single intravitreal injection.

2. Methods

2.1. Chemicals

Phosphatidylserine (PS) and 10-carboxymethyl-9-acridanone (CMA) were bought from Sigma-Aldrich, USA. C176 was purchased from Selleck, China. Cetyltrimethyl ammonium chloride (CTAC) and cholesterol were purchased from Aladdin, China. Triethanolamine (TEA) was gained from Macklin, China. Tetraethoxysilane (TEOS) was bought from Sinopharm Chemical Reagent Co., Ltd., China. Soybean phospholipid was purchased from Shanghai Yuanye Bio-Technology Co., Ltd. 1,2-distearoyl-*sn*-glycero-3-phosphoethanolamine-polyethylene glycol (DSPE-PEG, Mw = 2000 Da) was purchased from Xi'an Ruixi Biological Technology Co., Ltd. 1′-dioctadecyl-3,3,3′,3′-tetramethylindodicarbocyanine,4-chlorobenzenesulfonate salt (DiD) was bought from Beyotime Biotechnology, China.

Unless otherwise noted, organic solvents and inorganic salts were purchased from Sinopharm Chemical Reagent Co., Ltd., China, and used without further purification. Water in all the experiments was purified using a Millipore-Q water-purification System (Milli-Q Integral 3, Millipore, USA).

2.2. Synthesis and characterization of DMSN

DMSN was prepared using the previous method [45]. In brief, 6 g CTAC was dissolved in 24 mL water, then 0.18 g TEA and 36 mL water were added, and stirred at 60 °C for 30 min at a stirring speed of 150 rpm. 2 mL TEOS was added to 18 mL cyclohexane, after which the solution was slowly added to the flask, continued to stir for 12 h. Precipitation was collected by centrifugation at 11000 rpm for 30 min. The template was removed by re-dispersed the precipitation in 20 mL methanol containing 1 % NaCl and reflux at 60 °C for 4 h. The DMSN precipitation was collected by centrifugation (11000 rpm, 30 min) and dispersed in water.

The hydrodynamic diameter and zeta potential of DMSN were determined by dynamic light scattering (DLS, Zetasizer 3000, Malvern, USA). Measurement was repeated three times to obtain an average value. The morphologies were observed under the transmission electron microscope (TEM, HT-7700, Hitachi, Japan) at 200 kV after placing a drop of the liposome solution on a copper grid coated with amorphous carbon. The scanning electron microscope (SEM, Hitachi S-4800 FESEM, Japan) was also applied to observe their morphologies.
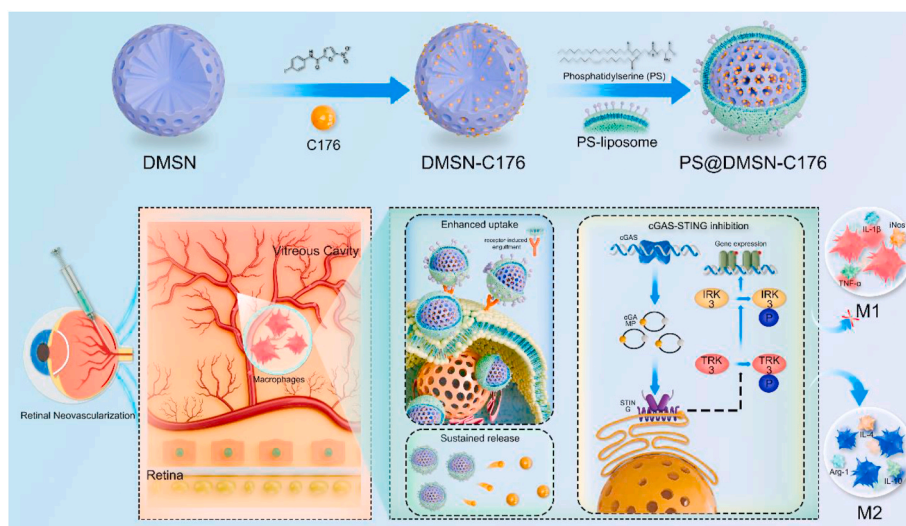
Scheme 1. The schematic illustration of the synthetic procedure and therapeutic mechanism of PS@DMSN-C176.

2.3. Preparation and characterization of DMSN-C176

The C-176 drug was dissolved in tetrahydrofuran (THF) to obtain different concentrations according to experimental requirements. 1 mL of C-176 solution with different concentrations was slowly added into 5 mL of 0.2 mg/mL DMSN aqueous solution, and stirred until THF was completely volatilized. Then, DMSN-C176 precipitation was collected by centrifuge (11000 rpm, 30 min). Extraction of C-176 from DMSN-C176 with dichloride and the extracted liquid was detected by an ultraviolet spectrometer (UV, UV2600, Shimadzu, Japan). In the meantime, the standard curve of C-176 was also obtained.

2.4. Synthesis and characterization of PS@DMSN-C176

Liposomes were prepared using the thin lipid film hydration method [46]. Briefly, 30 mg of PS, 10 mg of cholesterol, and 10 mg of DSPE-PEG were dissolved in 10 mL of chloroform, which was referred to as PS solution. 30 mg of soybean phospholipid, 10 mg of cholesterol, and 10 mg of DSPE-PEG were dissolved in 10 mL of chloroform, referred to as lipid solution. After adjusting the ratio of PS solution to lipid solution at 2:1, 0.4 mL of the above solution (5 mg/mL) and 8 mL of chloroform were added into a round flask and slowly evaporated to form a thin film by rotary evaporator at 40 °C. Then, 1 mL of 1 mg/mL DMSN-C176 was added to the round flask and sonicated for 20 min in an ice water bath to obtain PS@DMSN-C176. Other NPs of different proportions of PS were obtained using the same method. 0 % PS-incorporated NPs were abbreviated as L@DMSN-C176. Fluorescent dye DID-loaded PS@DMSN was gained by adding 10 μL 1 mg/mL DID solution.

The hydrodynamic diameter and zeta potential of all liposomes were determined by DLS. The morphologies were observed under TEM by using a phosphotungstic acid solution (2 %) to stain the sample on a copper grid. Fourier Transform infrared spectroscopy (FTIR, Nicolet 6700, Thermo Fisher Scientific, USA) was used to detect the characteristic functional groups in the range 4000-400 cm-1 by using KBr pellet method. X-ray photoelectron spectroscopy (XPS, ESCALAB 250Xi, Thermo Scientific, USA) was measured based on the C1s line at 284.6 eV as a reference. The drug in PS@DMSN-C176 was extracted with dichloride and the extracted liquid was detected by an ultraviolet spectrometer to determine the loaded drug amount.

2.5. Drug release manner of PS@DMSN-C176

1 mL PS@DMSN-C176 was packed in a dialysis tubing (MWCO = 3500 Da) and placed in 10 mL PBS (pH 7.4) at 37 °C water bath with orbital shaking at 200 rpm. At predetermined time intervals, the PBS was removed followed by adding free 10 mL of PBS. The drug release amount was determined by UV.

2.6. Cell uptake of PS@DMSN-C176

DID-loaded PS@DMSN with 0 %, 20 %, 40 % of PS were obtained using the abovementioned methods. The fluorescence intensity (FI) of 1 μg/mL NPs was measured by a multifunctional microplate reader (FI^x, x = 0 %, 20 %, 40 %). RAW264.7 cells were incubated with DID-loaded PS@DMSN with different proportions of PS for 6 h and then collected and analyzed by flow cytometry to obtain the value of mean fluorescence intensity (MFI^x). The phagocytic ratios were calculated as follows:

$$Phagocytic\ Ratio = \frac{MFI^x/FI^x}{MFI^{0\%}/FI^{0\%}}$$

The representative images of cell uptake at different times were obtained by confocal microscope with the co-staining of CMFDA (Invitrogen, C2925) and Hochest.

2.7. Cell experiments

RAW264.7 cells were purchased from the Cell Bank of the Chinese Academy of Sciences (Shanghai, China). Cells were plated in 6-well culture plates in Dulbecco's Modified Eagle Medium (DMEM, Gibco, USA) supplemented with 10 % fetal bovine serum (FBS) and 1 % penicillin/streptomycin at 37°C in an incubator with 5 % CO2. To mimic the macrophage polarization profile during the early stage of OIR, cells were incubated with 100 ng/mL lipopolysaccharide (LPS) for 12 h and then treated with PBS, C176, DMSN, DMSN-C176, L@DMSN-C176, PS@DMSN-C176 (containing 1 μM C176 for both free drug and NPs released drug) for 12h. To mimic the activation of the cGAS-STING pathway during OIR, cells were incubated with 10 nM CMA for 2 h and then treated the same way as before. The cells were then harvested for western blotting, qRT-PCR, and immunofluorescent staining.

2.8. Animal models

Wild-type neonatal C57BL/6J mouse pups were purchased from the Animal Center at the author's institute. The induction of OIR was performed as previously described [47]. In brief, litters of neonatal mouse pups were exposed to 75 % O$_2$ from postnatal day 7(P7) to P12, then returned to room air until P17 [48]. Pups from the same litter were randomly assigned to different treatment groups to minimize the

differences in weight between litters. Both male and female pups were used for the study.

2.9. Intravitreal injection

At P12, neonatal mice were anesthetized with 2 % isoflurane. One drop of proparacaine hydrochloride on the cornea's surface achieved topical anesthesia. The iris was dilated by using tropicamide phenylephrine eyedrops. Afterward, mice were intravitreally injected with 1 μL of 10 μM C176 in NPs and PBS (DMSN, DMSN-C176, L@DMSN-C176, PS@DMSN-C176 with 10 μM C176 released) using a 33-gauge Hamilton needle and syringe (Hamilton Company, Germany) under the surgical operation microscope. Mice treated with 1 μL intravitreal injection of 10 mM PBS were regarded as the OIR group.

2.10. Immunofluorescent staining

At P17, mice were sacrificed and the eyeballs were enucleated, embedded in optimal cutting temperature (OCT) compound, and sectioned to 8 μm on a Leica cryostat (Buffalo Grove, IL). For immunofluorescent staining, cryosections were fixed in 4 % paraformaldehyde for 20 min, then permeabilized and blocked in PBS containing 10 % goat serum and 0.2 % Triton-X-100 for 1 h. The slides were then incubated with primary antibodies against rat F4/80 (1:100, Abcam, ab6640), rabbit IRF3 (1:100, HuaBio, ET1612-14) overnight at 4 °C. After washes, slides were incubated with Alexa-488, Alexa-555-conjugated secondary antibody (1:1000, 4412S, 4417S, Cell Signaling Technology) for 1 h at room temperature. Before imaging, the slides were counterstained with 4′,6-diamidino-2-phenylindole (DAPI).

For whole-mount retinal immunofluorescence, eyeballs were enucleated and fixed in 4 % paraformaldehyde for 2 h at room temperature. Retinas were then carefully dissected, blocked, and permeabilized in PBS containing 10 % goat serum, 3 % BSA, 1 % Triton-X-100, and 0.2 % Tween 20 for 1 h as previously reported [16]. Afterward, retinas were incubated with primary antibody against rat F4/80, rabbit IL-10 (1:100, Abcam, ab9969), mouse TNFα (1:100, Abcam, ab1793), and Alexa-568-labeled Griffonia simplicifolia isolectin B4 (10 μg/mL, I21411, Invitrogen) overnight at 4 °C. On the next day, the primary antibodies were washed and retinas were incubated with Alexa-488, Alexa 405-conjugated secondary antibody (1:1000, 4408S, 4412S, Cell Signaling Technology; 1:1000, ab175671, Abcam) for 1 h at room temperature. Retinas were then flat-mounted on microscope slides.

For cell samples, cells were fixed in 4 % paraformaldehyde for 20 min, then permeabilized and blocked in PBS containing 10 % goat serum and 0.2 % Triton-X-100 for 1 h. Afterward, cells were incubated with primary antibody mouse TNFα, rabbit IL-10 and rabbit IRF3 overnight at 4 °C. After washes, cells were incubated with corresponding secondary antibodies for 1 h at room temperature. Before imaging, cells were counterstained with DAPI.

A confocal microscope and an inverted fluorescence microscope imaged cryosections, flat-mounted retinas, and cell samples. The intensity of fluorescence and the avascular and neovascular areas (defined as a percentage of total retinal areas) were quantified using ImageJ by researchers blinded to experimental conditions as previously described [47].

2.11. Flow cytometry analysis

RAW264.7 cell samples were collected and incubated in CD16/CD32 antibody (1:100, BD Pharmingen, 553141) for blocking Fc receptors at room temperature for 20 min. Samples were then fixed with fixation and permeabilization buffer (BD Pharmingen, 55471) at 4 °C for 20 min, followed by incubation with fluorescence-conjugated antibodies against Inos and CD206 (1:100, Biolegend, 696805; 1:100, Invitrogen, 2324842) for 30 min. After staining, samples were analyzed by a BD FACS LSRFortessa flow cytometer (BD Pharmingen) and Flow Jo

software.

2.12. qRT-PCR

RNA from cell samples and whole retinas were extracted by using FlaPure Animal Tissue Total RNA Extraction Kit (Genesand Biotech Co., Ltd). Using the reverse transcription kit, the extracted RNA was used as the template to generate cDNA (Takara, RR036A). qRT-PCR was performed on a StepOne Plus System (Applied Biosystems) using TB Green Premix Ex Taq (Takara, RR420a) with the primers given in Table S1.

2.13. Western blot analysis

Retinas and cell samples were lysed in RIPA buffer (Beyotime, P0013) containing 2 % proteinase inhibitor (Beyotime, P1008), 1 % phosphatase inhibitor cocktail (Selleck, B15001) and 1 % Phenylmethanesulfonyl fluoride for 30 min. After brief sonication, the samples were centrifuged at 12,000 g for 10 min at 4 °C. Protein concentrations of the supernatant were determined by BCA assay (Beyotime, P0012). Samples with equal amounts of total proteins were resolved in SDS-PAGE gels and transferred to PVDF membranes. After blocking with quick-blocking buffer (Beyotime, P0252), the membranes were incubated with primary antibodies including STING (CST, 50494), phosphorylated STING (p-STING, CST, 72971), TBK1 (CST, 3504), phosphorylated TBK1 (*p*-TBK1, CST,5483), IRF3 (Huabio, ET1612-14), phosphorylated IRF3 (*p*-IRF3, CST, 4947), albumin (Proteintech, 16475), vascular epithelial growth factor (VEGF, Santa Cruz Biotechnology, sc-7269), β-Tubulin (Proteintech, 66240), overnight at 4 °C, followed by incubation with secondary antibodies (CST, 7076; Proteintech, SA00001) for 1 h. All antibodies were diluted in universal antibody diluent (NCMbiotech, WB500D). Protein expression was semiquantified using ImageJ and the expression levels of target proteins were expressed relative to β-actin.

2.14. Enzyme-linked immunosorbent assay (ELISA)

The levels of pro-inflammatory cytokines IL-1β, IL-6 and anti-inflammatory cytokine IL-4

in the supernatants of RAW264.7 cells after incubation with 1 μg/ml LPS and drugs were quantified using the mouse ELISA kits (mlbio, ml063159, ml301814, ml063156) as per the manufacturer's instructions.

2.15. Neovascular nuclei quantification

Retinal sections containing the central area of the retina were selected and stained with hematoxylin-eosin (H&E). These sections were then scanned by a KF-PRO-100 scanner (KFBio) to generate the digital whole-slide pathological images. RNV was evaluated by counting the number of neovascular nuclei that protruded into the vitreous cavity as previously described [49]. The counting process was conducted in the K-Viewer software by an investigator blinded to the group assignment.

2.16. Toxicity evaluation

In vitro, the Cell Counting Kit 8 (CCK8, beyotime) was used to measure the viability of RAW 264.7 cells after incubating in C176 and PS@DMSN-C176 with different concentrations following the instructions. Besides, a live/dead cell viability assay was performed after the incubation of RAW264.7 cells in DMSN, DMSN-C176, L@DMSN-C176, PS@DMSN-C176 group, and C176 group (diluted in DMSO) for 24 h. A confocal microscope captured the representative images of groups.

In vivo, C57BL/6J mice were intravitreally injected with 1 μL of 10 mM PBS and PS@DMSN-C176 (10 μM C176) at P12. Blood routine, blood biochemical, and histopathology assays were examined at P17

including the levels of alanine aminotransferase (ALT), aspartate aminotransferase (AST), blood urea nitrogen (BUN), creatinine (CRE), red blood cell count (RBC), white blood cell count (PLT), neutrophil count (Neu), lymphocyte count (Lym) and the examination of the H&E staining sections of the heart, liver, spleen, lung, and kidney.

2.17. Statistical analysis

Data were expressed as mean ± standard deviation (SD). The data analysis was performed using GraphPad Prism 7.0 Software (GraphPad Software Inc., USA). The differences between the two groups were evaluated with t-test and the differences between multiple groups were evaluated with One-way ANOVA. The significance level was presented as *$P < 0.05$, **$P < 0.01$, ***$P < 0.001$ and ****$P < 0.0001$, respectively.

3. Results and discussion

3.1. Physiochemical properties of DMSN-C176

DMSN was prepared by condensation of silica precursors TEOS in the presence of cationic surfactants CTAB as a structure-directing template under basic conditions [45]. The morphology of DMSN was analyzed by transmission electron microscopy (TEM) as shown in Fig. 1A, which showed that sphere-like NPs have a dendrimer-like wrinkled structure. These spherical wrinkled structures provide easy drug loading. The size of DMSN detected by DLS was 92.3 ± 5.4 nm with PDI of 0.191 (Fig. 1C), which was consistent with TEM images. Then, the drug-loaded microspheres were prepared by solvent volatilization method. To further optimize the encapsulation efficiency of C176, we altered the feeding ratios of drugs and DMSN. Under the premise of 5 mL 0.2 mg/mL carrier, 1 mL C176 with different concentrations was added. As shown in Fig. 1E, when the concentration varied from 100 to 300 μg/mL, the drug loading and encapsulation efficiency was gradually increased, which demonstrated 14.87 % of loading efficiency and 58.29 % of encapsulation

efficiency at 300 μg/mL feeding. Further increasing the C176 feeding concentration up to 500 μg/mL, the loading efficiency was not significantly changed while the encapsulation efficiency was dropped. Thus, 300 μg/mL C176 feeding concentration was selected to prepare the drug-loaded NPs for subsequent experiments. The calibration curve of C176 is shown in Fig. S1.

3.2. Cell uptake and cellular toxicity of PS@DMSN-C176

Resident or infiltrated macrophages are the main initiators of the inflammation in the retina microenvironment, which regulate the immune response, synaptic pruning and axonal growth by phagocytosis [50,51]. To maximize the drug effect on macrophages in the retina, we expected to increase cell uptake of NPs by macrophages. PS was selected as the shell of DMSN because the externalization of PS on the cell membrane is a major "eat-me" signal for macrophages to trigger cell uptake. To determine the optimal incorporation ratio of PS, we prepared the lipid shells in which PS components accounted for 0 % (L@DMSN-C176), 20 % and 40 % of the total phospholipid components. RAW264.7 mouse macrophages can perform phagocytosis and pinocytosis, and can effectively respond to in vitro stimuli by polarizing to different subtypes [52–54]. Thus, RAW264.7 cells were used for assessing the cell uptake as well as phenotypic transformation in this study. After incubation with 0, 20 % and 40 % PS@DMSN for 6 h, the phagocytic ratios were 1.00 ± 0.08, 1.61 ± 0.06, 3.48 ± 0.09 (Fig. 2A). The representative cell uptake images of NPs with different PS ratios are shown in Fig. 2D, which was consistent with quantitative data by flow cytometry. In addition, the phagocytosis of NPs by cells was time-dependent (Fig. 2B). According to the above results, 40 % PS incorporation ratio was chosen to prepare PS@DMSN-C176. As illustrated in Fig. 1B, the mesoporous structure of PS@DMSN-C176 could still be observed but slightly blurred, indicating that the phosphorus layer covered the surface of DMSN. SEM images were also carried out, which showed less pore structure of PS@DMSN-C176 on the surface (Fig. S10). Additionally, the FTIR spectrum and XPS curve indicated the
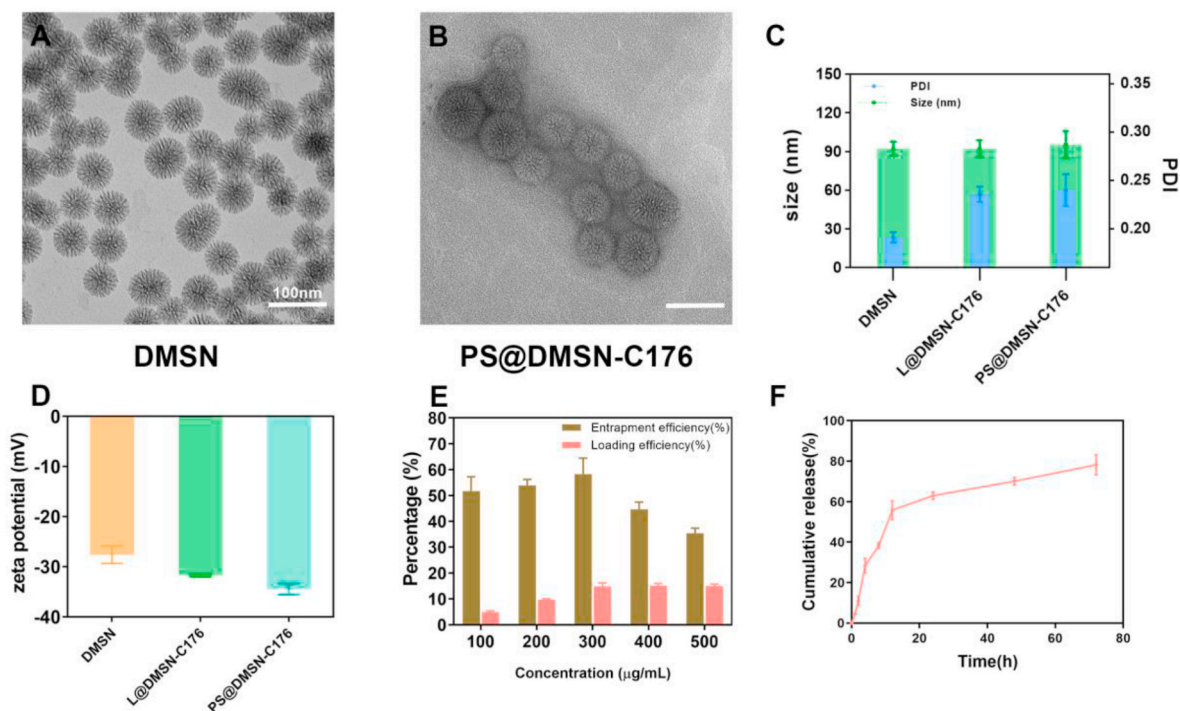
Fig. 1. The characterization of PS@DMSN-C176. TEM images of (A) DMSN and (B) PS@DMSN-C176. (C) Hydrodynamic diameter and (D) Zeta potential of DMSN, L@DMSN-C176 and PS@DMSN-C176 measured by DLS (n = 3). (E) The entrapment efficiency and loading efficiency with different C176 feeding concentrations (n = 3). (F) Cumulative release of C-176 from PS@DMSN-C176 NPs (n = 3). Data were presented as mean ± SD.
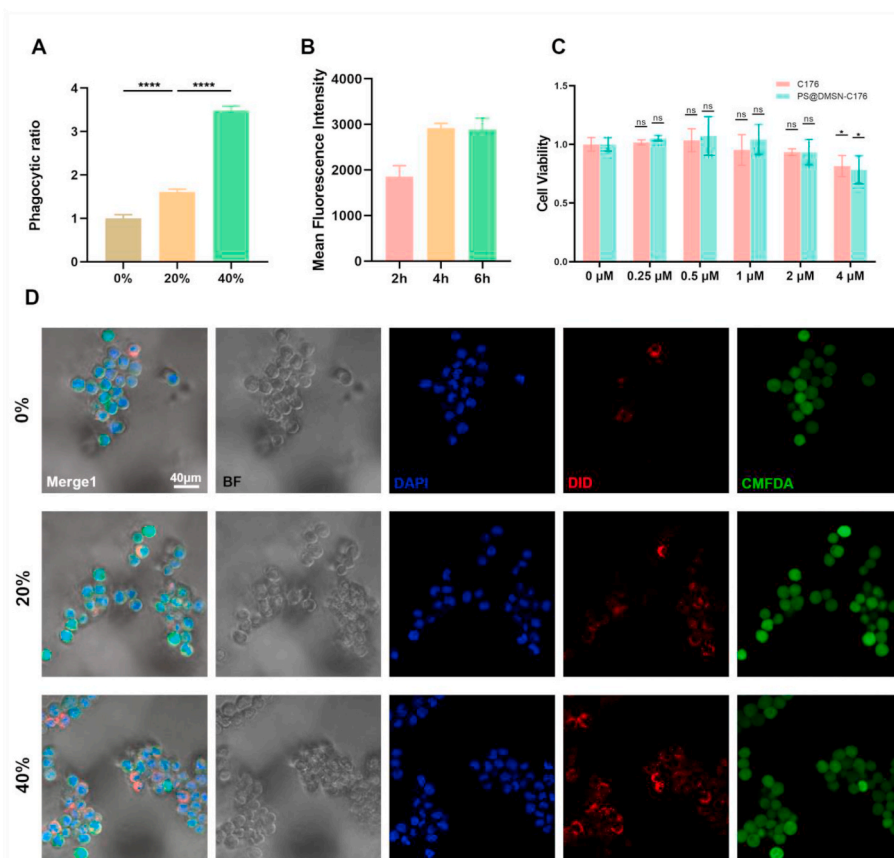
Fig. 2. Cell uptake and cytotoxicity of PS@DMSN-C176. (A) Phagocytic ratios of PS@DMSN-DID contain 0 %, 20 % and 40 % PS (n = 3). (B) Mean fluorescence intensity of cells after incubation with PS@DMSN-DID for 2 h, 4 h and 6 h (n = 3). (C) Cell viability of RAW264.7 cells incubated with different concentrations of PS@DMSN-C176 for 24 h (n = 3). (D) Representative images of cell uptake after 6 h incubation with PS@DMSN-DID. Data were presented as mean ± SD. ns means no significant difference. *p < 0.05, ****p < 0.0001.

successful loading C176 and coating PS liposomes (Figs. S11 and S12). The particle size of PS@DMSN-C176 and L@DMSN-C176 tested by DLS was 95.34 ± 10.58 nm (PDI = 0.240) and 92.22 ± 6.5 nm (PDI = 0.234), respectively (Fig. 1C). The zeta potentials of these NPs were all close to −30 mV, indicating good stability (Fig. 1D, Fig. S13). It was worth noting that the coating process of PS liposomes on DMSN-C176 did not affect the drug content in DMSN-C176 (Fig. S14).

Since biocompatibility is essential for the deployment of nano-materials, an in vitro evaluation was initially carried out. The viability of RAW 264.7 cells incubated with different concentrations of C176 and PS@DMSN-C176 showed the PS@DMSN-C176 at a lower concentration than 4 μM was biosafe (Fig. 2C). The representative images of a live/dead cell viability assay were illustrated in Fig. S2, demonstrating that there is no obvious cell death after incubated with 1 μM C176, DMSN, DMSN-C176, L@DMSN-C176 and PS@DMSN-C176 for 24 h. The above results demonstrated that 1 μM C176 and PS@DMSN-C176 have no toxicity to RAW 264.7 cells.

3.3. Drug release manner of PS@DMSN-C176

The cargo release capacity of PS@DMSN-C176 was in addition to that studied. As demonstrated in Fig. 1F, the typical slow-release manner of PS@DMSN-C176 at pH 7.4 PBS solution can be observed, which released nearly 60 % of the drug in the first 24 h, and then the drug release rate was further slowed down within 12 h–72 h. Finally, at the time mark of 72 h, 78.22 % of drugs were released from PS@DMSN-C176.

3.4. PS@DMSN-C176 attenuate inflammation by promoting M2 polarization in vitro

Once macrophages in the retina are activated as the M1 proinflammatory state, they start secreting related cytokines that cause acute inflammation. The intervention of PS@DMSN-C176 was expected to reverse the M1 polarization to M2, thereby attenuating the inflammation [20,55]. LPS was used to mimic the M1 polarization of macrophages during OIR, evidenced by the proportion of iNOS + CD206- (M1 marker) cells increasing from 0 % to 40.1 % while the proportion of CD206+iNOS- (M2 marker) cells slightly changes from 4.5 % to 6.3 %. After treating with DMSN-C176 or L@DMSN-C176, M2 polarization was increased from 4.5 % to 14.7 % and 12.1 %, and M1 polarization was decreased from 40.1 % to about 26 % while the M2 polarization was boosted to 21 % and the M1 polarization was dropped to 19 % in C176 or PS@DMSN-C176 group (Fig. 3A–C). The relatively low curative effect for DMSN-C176 or L@DMSN-C176 than C176 and PS@DMSN-C176 groups indicated that the 1 μM C176 is in its optimal effective range, and the slow-release properties of NPs allow the drug to gradually reach its effective value, thus reducing the efficacy. Additionally, PS@DMSN-C176 achieved the same therapeutic effect as C176 did due to the enhanced uptake of PS@DMSN-C176, which laterally proved the promoting endocytosis effect of PS. Moreover, the expression of inflammatory factors is another indicator of inflammation. As shown in Fig. 3D–G, the anti-inflammatory genes levels of Arg-1 and IL-4 in C176 and PS@DMSN-C176 groups were most upregulated among those groups while the expressions of inflammatory IL-1β and IL-6 were decreased by the same trend. ELISA results of IL-1β, IL-6 and IL-4 were
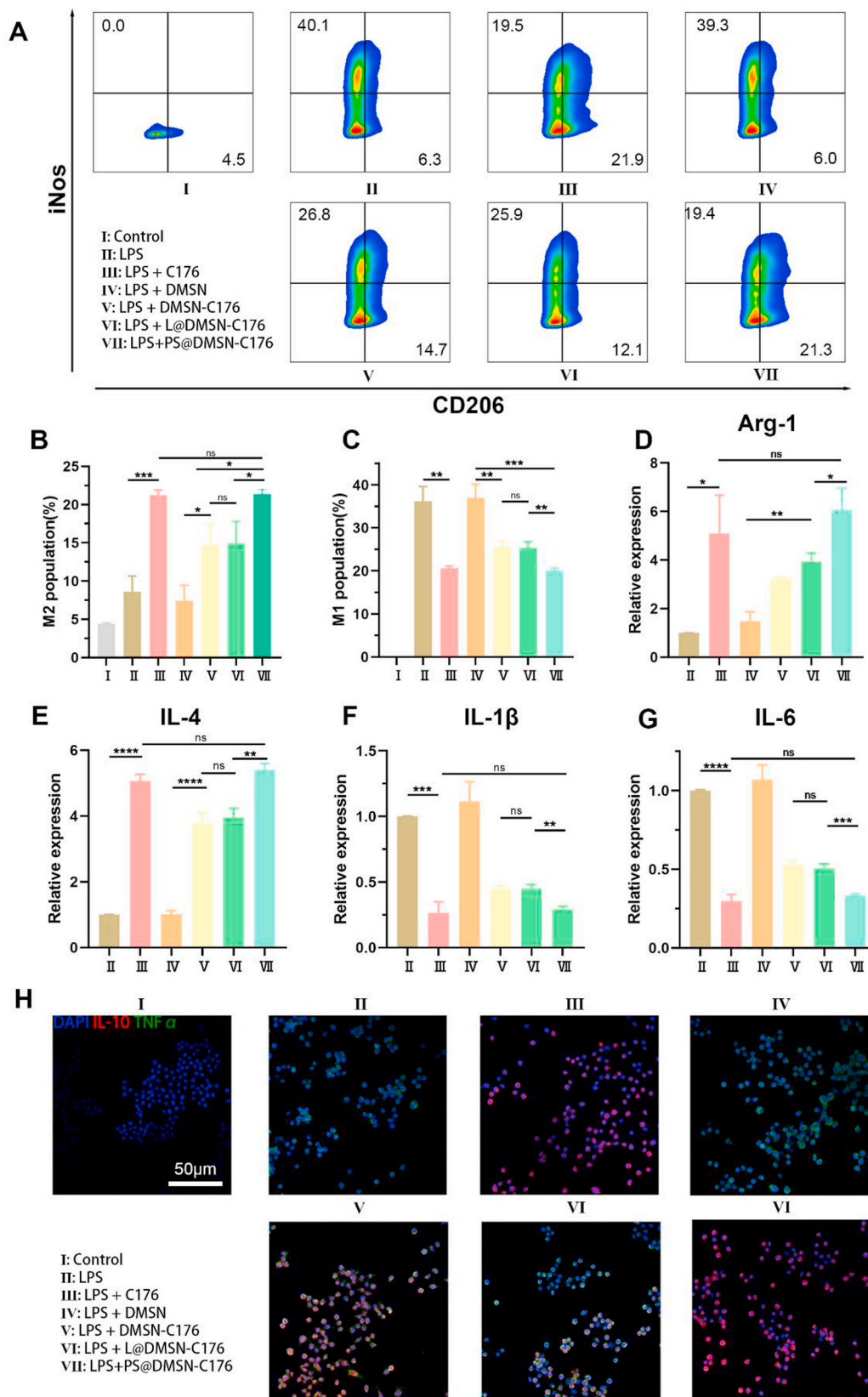
Fig. 3. PS@DMSN-C176 promotes the M2 polarization and inhibits M1 polarization in vitro. (A) Typical flow cytometry data and corresponding quantification of (B) iNos + CD206- (M1 marker) and (C) iNos-CD206+ (M2 marker) cell populations after LPS stimulation and indicated treatments (n = 3). The mRNA expression levels of anti-inflammatory cytokines (D) Arg-1, (E) IL-4, and pro-inflammatory cytokines (F) IL-1β, (G) IL-6. (H) Immunofluorescence of IL-10 and TNFα in RAW264.7 cells (n = 3). Data were presented as mean ± SD. ns means no significant difference. *p < 0.05, **p < 0.01, ***p < 0.001, ****p < 0.0001.

also consistent with the expression trend of the corresponding genes (Fig. S15). Fig. 3H also showed that cells produced less pro-inflammatory cytokines (TNFα) and more anti-inflammatory cytokines (IL-10) after the treatment, and it was more prominent in C176 and PS@DMSN-C176 groups.

3.5. PS@DMSN-C176 effectively inhibits the cGAS-STING pathway in vitro

Recently, it was found that infiltrating and resident macrophages in retinal neovascularization tissues express high levels of cGAS and STING, which was highly correlated with the polarization of macrophages [22]. To mimic the activation of the cGAS-STING pathway during OIR, we use CMA as the agonist of this pathway to stimulate RAW264.7 cells. From the Western blot results illustrated in Fig. 4A–F,
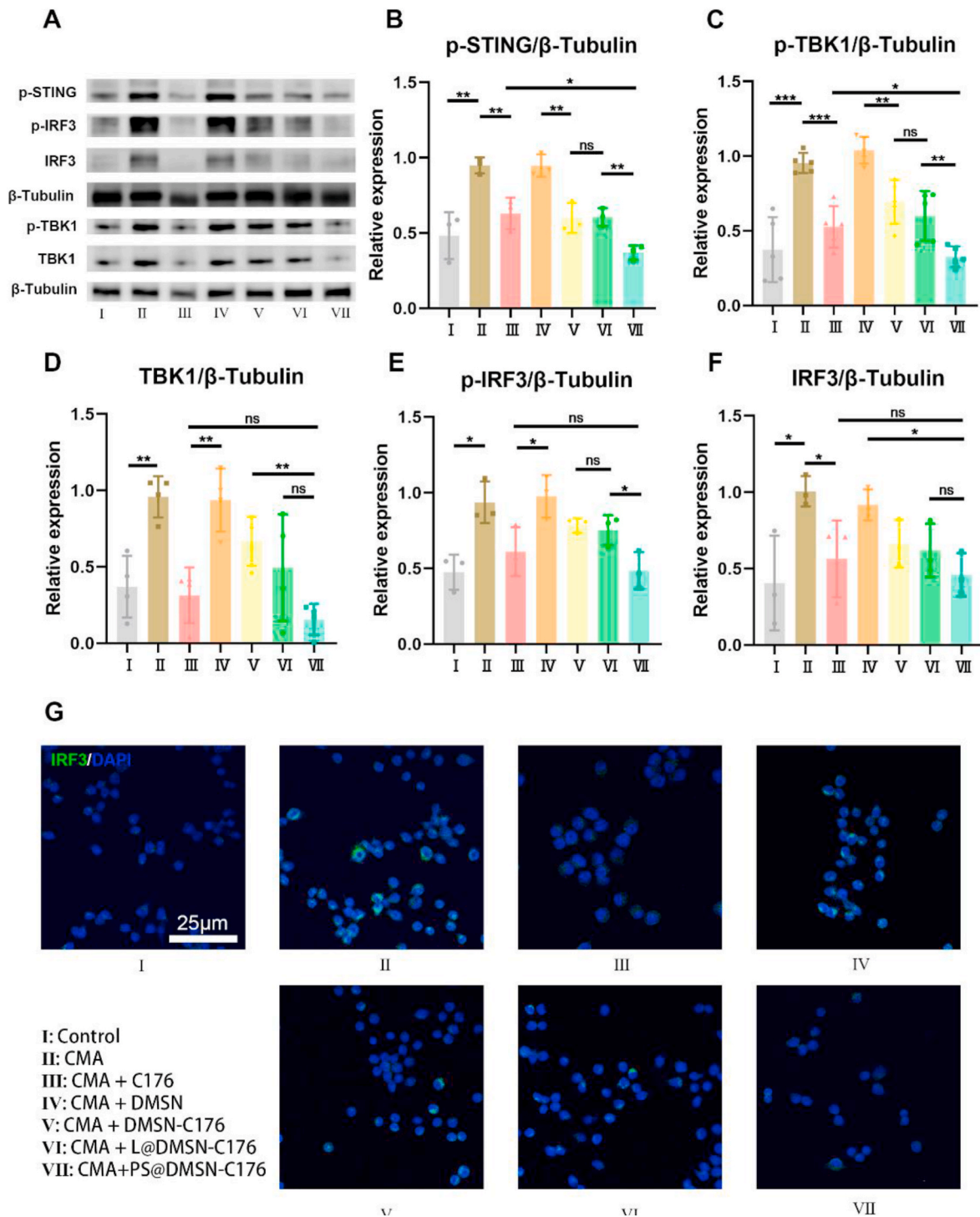
Fig. 4. PS@DMSN-C176 inhibits cGAS-Sting pathway in vitro. (A) Western blot and protein levels of (B) p-STING, (C) *p*-TBK1, (D) TBK1, (E) *p*-IRF3, (F) IRF3 in RAW264.7 cells quantified by densitometry and normalized by β-tubulin levels (n = 3 to 5). (G) Immunofluorescence of IRF3 in Raw264.7 cells after different treatments. Data were presented as mean ± SD. ns means no significant difference. *p < 0.05, **p < 0.01, ***p < 0.001.

C176, and PS@DMSN-C176 effectively inhibited the activation of the cGAS-STING pathway in RAW264.7 cells. The expression of p-STING and *p*-TBK1 treated with PS@DMSN-C176 was even lower than in the C176 group, and the expression of TBK1, IRF3, and *p*-IRF3 showed no statistical differences between the two groups, indicating that the inhibitory effect may be slightly stronger when treating with PS@DMSN-C176. Due to the enhanced cell uptake, the inhibitory effect of DMSN-C176 and L@DMSN-C176 was weaker than PS@DMSN-C176. As illustrated in Fig. 4G, IRF3 expression was inhibited after the incubation with C176 and NPs, which was consistent with the Western blot results.

3.6. PS@DMSN-C176 alleviates oxygen-induced retinopathy

During retinal vasculature development, some external influences (such as increased oxygen concentrations) can disturb normal angiogenesis. In humans, the retinal vasculature development is completed by birth. Preterm infants with supplemental oxygen treatments will probably suffer from the arrest of normal retinal vessel growth, neovascularization, and finally blindness, which is called the retinopathy of prematurity [10,56]. However, in mice and rats, the retinal vasculature develops after birth, forming the basis of the OIR model. The increased tissue oxygenation (75 % oxygen) from P7 to P12 leads to vaso-obliteration in the retinal non-perfusion central area and the relative hypoxic environment (room air) from P12 to P17 triggers the RNV (Fig. 5A).

Above all, we studied the effective concentration of PS@DMSN-C176 in vivo. First, PS@DMSN-C176 with 1 μM, 5 μM or 10 μM released C176 showed no retinal pathological manifestations from the H&E staining of the retinal sections (Fig. S3), indicating that these three doses are within the safe range. Besides, we assessed the blood biochemical values and blood routine indexes to confirm the biosafety of intravitreal administration of PS@DMSN-C176 containing 10 μM released C176, which showed no difference from healthy mice in BUN, AST, ALT, and CRE items. (Fig. S4). Besides, no abnormality was found on the heart, liver, spleen, lung and kidney according to the results of H&E staining (Fig. S4). These results indicated that PS@DMSN-C176 was biosafe enough to treat OIR. Since diseased vascular tufts can penetrate the inner limiting membrane and grow towards the vitreous, the severity of retinopathy can be assessed by calculating the proportion of vaso-obliteration areas and the neovascularization areas in flat-mounted images and the number of neovascular nuclei in retinal sections. As illustrated in Fig. S5, the mean proportions of vaso-obliteration in OIR, 1 μM, 5 μM, and 10 μM groups were 29.8 ± 7.5 %, 18.7 ± 4.1 %, 14.4 ± 1.9 % and 10.6 ± 3.3 %, respectively, while the mean proportions of neovascularization were 13.1 ± 3.0 %, 11.3 ± 2.7 %, 9.2 ± 1.0 % and 4.5 ± 1.6 %, respectively. The pathology present in flat-mounted images was alleviated most in the 10 μM group. Consistent with the above results, the expression of IL-1β in retinas was reduced after treatment with PS@DMSN-C176 and the 10 μM group decreased most (Fig. S6). In summary, PS@DMSN-C176 containing 10 μM released C176 was used for the following animal experiments.

We further compared the therapeutic effects of each component of PS@DMSN-C176. The representative flat-mounted images, retinal section images and bright field images of different treatments were illustrated in Fig. 5B and C and Figs. S7 and S9. Opposite from the solid anti-inflammatory effects in vitro, free drug C176 did not show any therapeutic effects according to the proportion of vaso-obliteration, neovascularization and the number of neovascular nuclei, which may be due to its hydrophobicity and possible agglomeration in the vitreous cavity or short tissue retention. Loading drugs into nanocarriers can help hydrophobic C176 disperse in water solution and achieve persistent release, and that made DMSN-C176, L@DMSN-C176 and PS@DMSN-C176 have therapeutic effects. Fig. 5D and E demonstrated that intravitreal injection with PS@DMSN-C176 had the most satisfactory therapeutic effects in decreasing the non-perfusion areas and

neovascularization areas while the therapeutic effects of DMSN-C176 and L@DMSN-C176 were lower than PS@DMSN-C176. Consistently, PS@DMSN-C176 prominently inhibited pathological angiogenesis by decreasing the number of neovascular nuclei compared to DMSN-C176 and L@DMSN-C176 (Fig. 5F) and the corresponding whole-slide pathological images were illustrated in Fig. S8. As VEGF is a key mediator of angiogenesis, and increased albumin in the retina is an indicator of vascular leakage, we conducted western blots to assess the expression levels of VEGF and albumin in different groups. As shown in Fig. 5G–I, the PS@DMSN-C176 group effectively decreased the expression of VEGF and albumin, indicating less neovascularization and vessel leakage. Likewise, free drug C176 did not change the protein expression in the retinas. However, after encapsulating it into DMSN or L@DMSN NPs, protein expression decreased, corresponding to the results of flat-mounted and retinal section images.
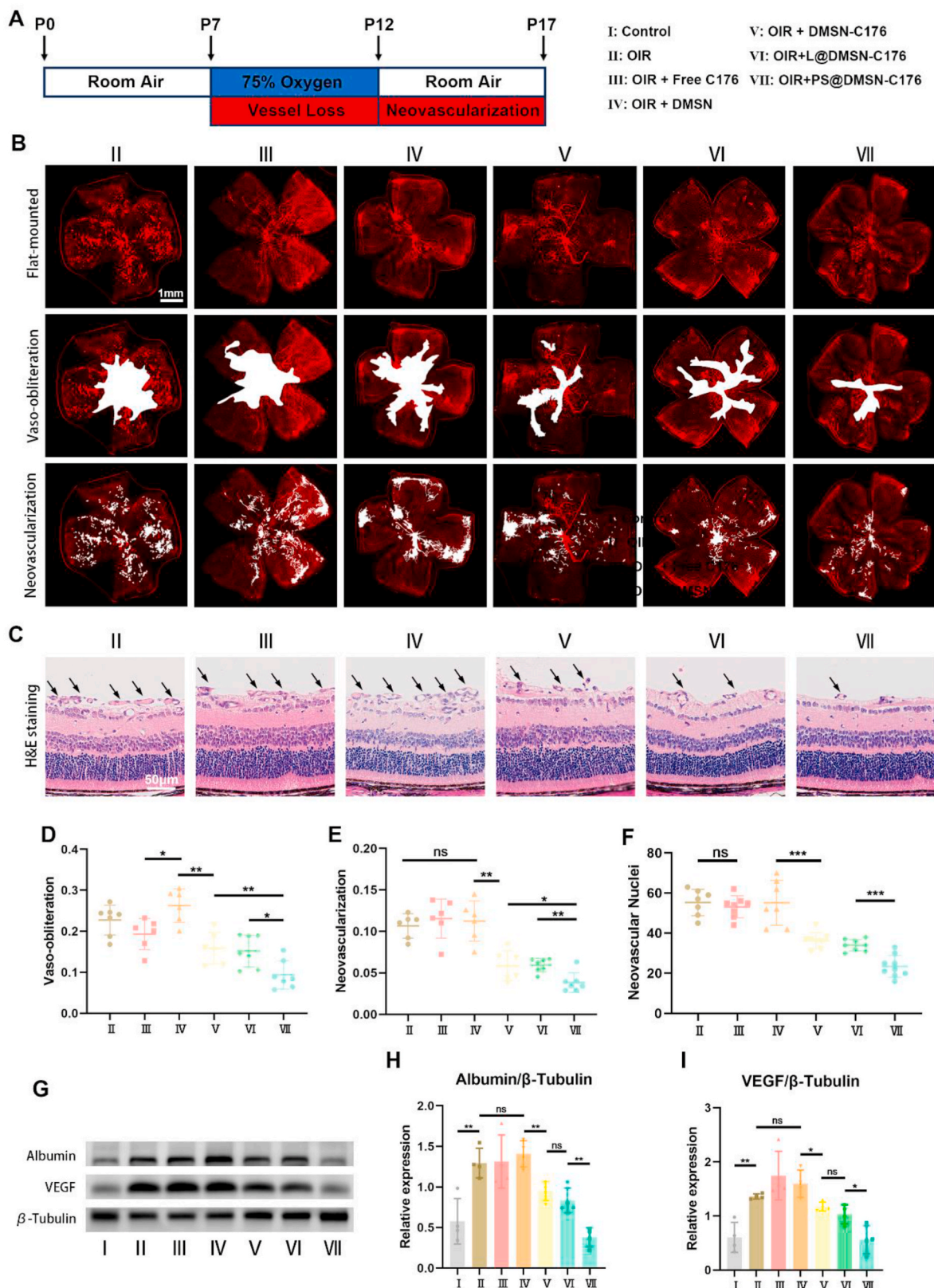
3.7. PS@DMSN-C176 attenuates retinal inflammation by promoting M2 polarization

As the proportion of the M1 state in macrophages is involved in the early stage of pathological angiogenesis in OIR mice, at the same time M2 phenotype may relieve inflammation and inhibit pathological angiogenesis. We studied the polarization of retinal macrophages after different treatments. By co-staining the flat-mounted retinas with IB4, f4/80, TNFα/IL10, we can find that the macrophages primarily distributed around/in the vessel they infiltrated or the leaky neovascular tissue from the representative flat-mounted images of different treating groups (Fig. 6A and C). The quantification of relative fluorescence intensity (TNFα/f4/80 area and IL-10/f4/80 area) was shown in Fig. 6B and D that PS@DMSN-C176 effectively inhibited the M1 polarization and promoted the M2 polarization of macrophages compared to other groups. We also assessed the expression of relative pro/anti-inflammatory genes in mice retinas. As illustrated in Fig. 6E–H, after treating with PS@DMSN-C176, the expression of pro-inflammatory factors such as IL-1β, IL-6, and iNos decreased significantly while the expression of anti-inflammatory index CD206 increased when compared to other groups, which was consistent with the immunofluorescent results.

3.8. PS@DMSN-C176 effectively inhibits cGAS-STING signaling in vivo

Next, we studied the inhibition effect of the cGAS-STING pathway in vivo by PS@DMSN-C176. The elevation of p-STING is a sign of activated cGAS-STING pathway. The immunoblot results validated the increased expression of p-STING and the phosphorylated level of STING in OIR mice retina, indicating the activation of the cGAS-STING pathway in the fundus. After intravitreal injection with PS@DMSN-C176, the pathway was inhibited, which was proved by the decreased retinal p-STING and phosphorylated level of STING. Due to the PS-modified liposomes, PS@DMSN-C176 showed the most potent inhibitory effect compared to DMSN-C176 and L@DMSN-C176 (Fig. 7A–C). Consistent with the immunoblot results, there was much less IRF3 expression in the retinal sections of PS@DMSN-C176 than other groups (Fig. 7D). Also, macrophages were mainly recruited to the ganglion cell layer in OIR and C176 groups due to the retinal neovascularization, and some macrophages penetrated the inner limiting membrane and located in the neovascular tufts.

In the present study, instead of blocking the VEGF pathway as the mainstream studies did, we successfully alleviated retinal neovascularization by reversing the M1 macrophages to M2 subtype at the early stage of OIR, because nonspecifically depriving normal growth of retinal endothelial cells may lead to serious adverse effects. Although there are studies reporting the pathological angiogenic effects of M2 polarization [57,58], in recent studies, the important role of M2 polarization in physiological angiogenesis is getting more and more emphasis. Wang et al. reported that M2-exosomes can promote M2

Fig. 5. PS@DMSN-C176 attenuates neovascularization, vaso-obliteration and vascular leakage in the OIR model. (A) The schematic illustration of the OIR model. (B) Representative images of IB4-stained retinal flat mounts and the corresponding vaso-obliteration areas and neovascular areas (white areas within retinas). (C) H&E staining and histological analysis of infiltration of neovascular nuclei in the OIR retinas. Black arrows indicate neovascular nuclei on the vitreal side of the inner limiting membrane. (D) and (E) Vaso-obliteration and neovascular areas quantified at P17 (n = 6 to 7). (F) Quantitative analysis of the number of neovascular nuclei in the OIR retinas at P17 (n = 7 to 9). (G), (H) and (I) Western blot and protein levels of albumin and VEGF in mice retina at P17 quantified by densitometry and normalized by β-tubulin levels (n = 4). Data were presented as mean ± SD. ns means no significant difference. $*p < 0.05$, $**p < 0.01$, and $***p < 0.001$.
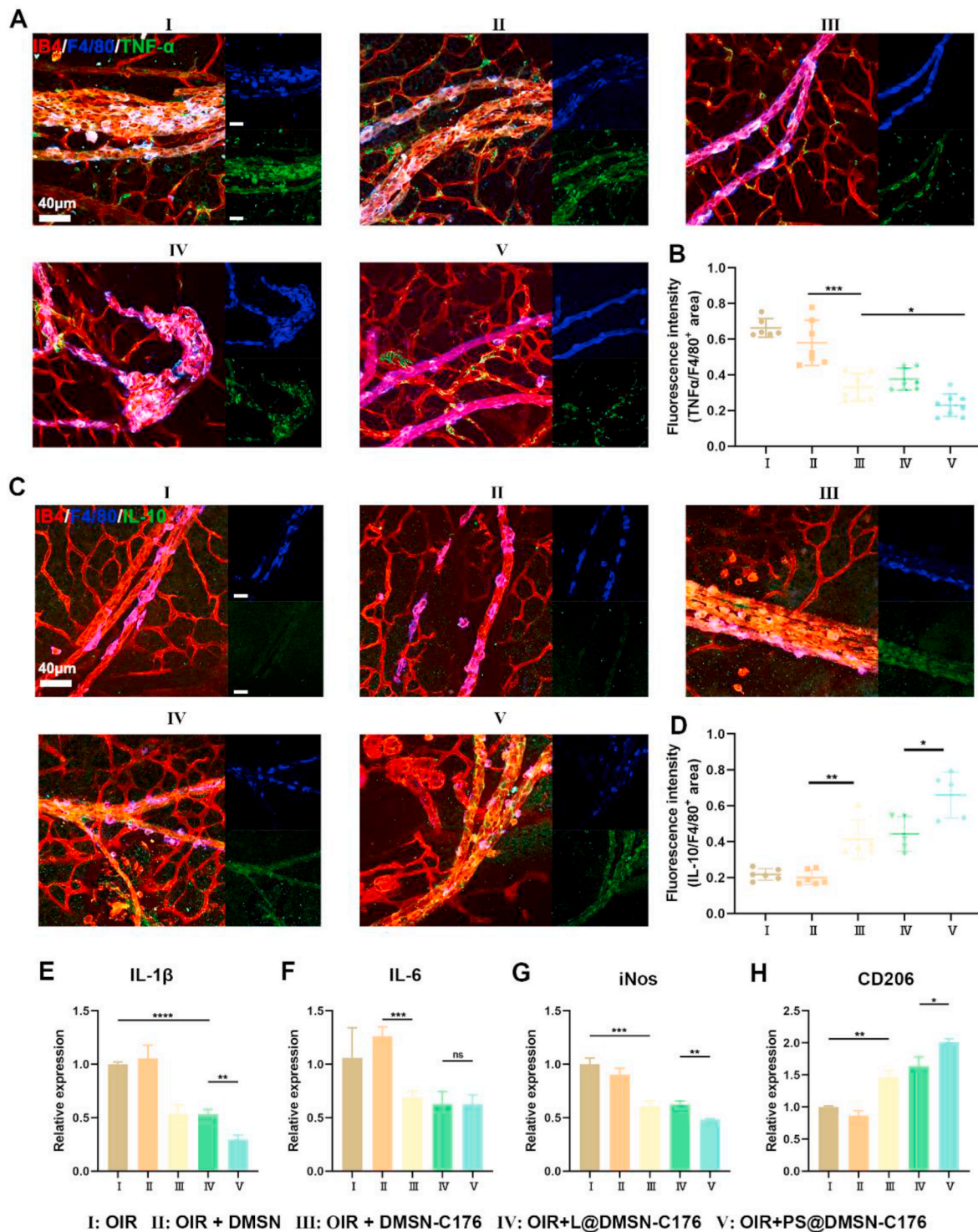
Fig. 6. PS@DMSN-C176 promotes M2 polarization and inhibits M1 polarization in vivo. (A) and (C) Representative images of retinal flat mounts stained with IB4, F4/80, TNF-α and IL-10. (B) and (D) Fluorescence intensity of F4/80, TNF-α, IL-10 staining was calculated by ImageJ software (n = 5 to 8). (E to H) qRT-PCR analysis of IL-1β, IL-6, iNos and CD206 mRNA levels in mice retina at P17 (n = 3). Data were presented as mean ± SD. ns means no significant difference. *p < 0.05, **p < 0.01, and ***p < 0.001.

polarization and induce retinal vascular remodeling in rodent models of OIR and diabetic retinopathy while Chen et al. found that M1-exosomes can activate resting microglia to M1 and amplifies pathological angiogenesis in OIR [21,59]. Besides, Huang et al. treated OIR with their miR-223-loaded and folic acid–chitosan-modified mesoporous silica nanoparticles by inducing M2 polarization, which further validated the therapeutic value of M2 macrophages [19]. Therefore, the definitive

role of pathological/physiological angiogenesis may not be very suitable for M2 macrophages on the topic of retinal neovascular diseases because the treatment of these diseases includes both the inhibition of pathological angiogenesis and the promotion of normal vessel formation. Given that inflammation is a well-known contributor to neovascularization, Xia et al. loaded rapamycin (an anti-inflammation agent) into the macrophage membrane-coated poly (lactic-*co*-glycolic)
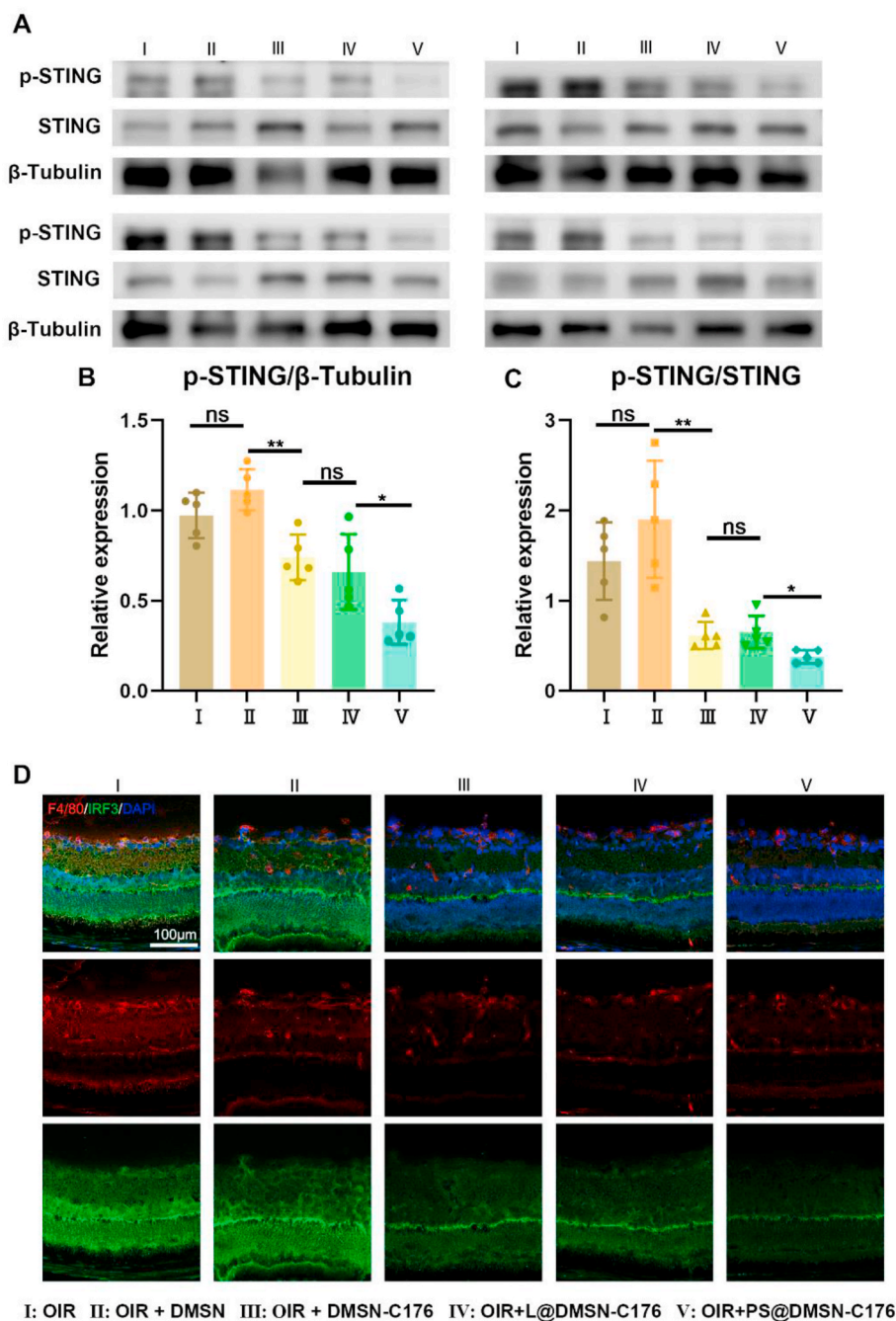
Fig. 7. PS@DMSN-C176 inhibits the cGAS-STING pathway in OIR mice retina. (A) Western blot and protein levels of (B) p-STING and (C) STING in mice retina at P17 quantified by densitometry and normalized by β-tubulin levels (n = 5). (D) Retinal sections of OIR mice stained with F4/80, IRF3 and DAPI. Data were presented as mean ± SD. ns means no significant difference. *$p < 0.05$, **$p < 0.01$.

acid nanoparticles to treat choroidal neovascularization (CNV) with 7 repeated intravenous dosages and Nguyen et al. encapsulated resveratrol and metformin into their nanoparticles to attenuate inflammation and oxidative stress for treating CNV [60,61]. In this study, we used PS-modified liposome carriers to promote C176 uptake which inhibited the intracellular STING, an overactivated inflammatory pathway in RNV. Moreover, the sustained release ability of DMSN and the biosafety with a high payload of C176 were also verified, making it possible to achieve satisfactory curative effects with a single dosage.

On selecting the way of drug administration, intravenous injections were indeed a much more accessible route as they don't require specialized equipment or personnel compared to intravitreal injections. Bohley et al. developed cyclosporin A–loaded lipid nanocapsules

outfitted with cRGD to treat ROP, which effectively delivers drugs to retina and inhibits retinal neovascularization with one intravenous dosage [62]. Nevertheless, with such a strategy to improve specificity and avidity for target cells, the study showed approximately only 10 % of the initial dose reached the fundus, indicating that it's a fairly challenging task to treat ROP with intravenous drugs. Li et al. successfully treated CNV using intravenous injections of fabricated hybrid cell-membrane-cloaked nanoparticles, but with repeated doses [63]. Given the above information, we decided to use direct intravitreal injections while the intravenous way remained to be further researched. Additionally, as there is no previous study reporting the intravitreal injection of drug C176, we examined the therapeutic effects of 3 groups with concentration gradients (1 μM, 5 μM, 10 μM) and selected the 10

μM group for our in vivo experiments.

In summary, we developed PS@DMSN-C176, which is designed for intravitreal injection to treat retinal neovascularization. PS@DMSN-C176 was characterized and served as a customized storage to slowly release C176 while the coated PS enhanced the drug uptake by macrophages. In vitro, we verified the M2 polarization from M1 induced by PS@DMSN-C176 with the stimulation of LPS and the blockade of the cGAS-STING pathway when macrophages were activated by CMA. In vivo, the therapeutic effects of PS@DMSN-C176 were quantified and superior when compared with free C176, DMSN, DMSN-C176 and L@DMSN-C176. The macrophage polarization profile and the inhibition of the cGAS-STING pathway were also assessed in vivo, which is consistent with the results in vitro. As silica is generally recognized as safe and small silica nanoparticles have been approved by the FDA for a human clinical trial [64–66], more researches are needed to decipher the therapeutic effects based on silica nanocarriers and accelerate the translation from the basic to the clinic.

4. Conclusion

The process of RNV is associated with the inflammation induced by acute M1 macrophage polarization. In this study, we targeted the STING of macrophages, a key mediator of inflammation, and effectively reversed the polarization from M1 to M2 subtypes by antagonist C176. By loading C176 into PS-modified DMSN, intravitreal administration of PS@DMSN-C176 demonstrated satisfactory biocompatibility, persistent release capacity, enhanced macrophage uptake, and strong STING inhibition, which contributed to a remarkable therapeutic effect on alleviating RNV in mice via one single dose. This study illustrated the long-lasting and macrophage-specific enhanced inhibition of the retinal inflammatory signaling pathway as a promising strategy for RNV treatments.

Conflicts of interest

None to declare.

Data availability

The data that support the findings of this study are included in this published article and supplementary materials. Additional data related to this paper may be requested from the authors.

Ethics approval and consent to participate

The study was approved by the Second Affiliated Hospital, Zhejiang University School of Medicine Ethics Committee (No 2021-0240) and adhered to the tenets of the Declaration of Helsinki.

CRediT authorship contribution statement

An Shao: Writing – original draft, Validation, Methodology, Investigation, Formal analysis, Data curation, Conceptualization. **Lulu Jin:** Writing – original draft, Validation, Methodology, Investigation, Formal analysis. **Yanni Ge:** Methodology, Formal analysis. **Ziqiang Ye:** Validation, Methodology. **Mingyu Xu:** Validation, Methodology. **Yifan Zhou:** Formal analysis. **Yingyu Li:** Methodology. **Linyan Wang:** Methodology. **Pinglong Xu:** Writing – review & editing. **Kai Jin:** Writing – review & editing, Methodology, Funding acquisition, Conceptualization. **Zhengwei Mao:** Writing – review & editing, Supervision, Methodology, Conceptualization. **Juan Ye:** Writing – review & editing, Supervision, Funding acquisition, Conceptualization.

Declaration of competing interest

The authors declare that they have no known competing financial interests or personal relationships that could have appeared to influence the work reported in this paper.

Appendix A. Supplementary data

Supplementary data to this article can be found online at https://doi.org/10.1016/j.bioactmat.2024.05.038.

References

[1] M.E. Hartnett, Pathophysiology and mechanisms of severe retinopathy of prematurity, Ophthalmology 122 (1) (2015 Jan) 200–210.

[2] T.Y. Wong, C.M.G. Cheung, M. Larsen, S. Sharma, R. Simó, Diabetic retinopathy, Nat. Rev. Dis. Prim. 2 (2016 Mar) 16012.

[3] N. Cheung, P. Mitchell, T.Y. Wong, Diabetic retinopathy, Lancet 376 (9735) (2010) 124–136.

[4] X. Li, G. Xu, Y. Wang, X. Xu, X. Liu, S. Tang, et al., Safety and efficacy of conbercept in neovascular age-related macular degeneration: results from a 12-month randomized phase 2 Study: AURORA study, Ophthalmology 121 (9) (2014) 1740–1747.

[5] J.S. Heier, D.M. Brown, V. Chong, J.F. Korobelnik, P.K. Kaiser, Q.D. Nguyen, et al., Intravitreal aflibercept (VEGF trap-eye) in wet age-related macular degeneration, Ophthalmology 119 (12) (2012 Dec) 2537–2548.

[6] A. Markham, Brolucizumab: first approval, Vol. 79, Drugs 79 (18) (2019 Dec) 1997–2000.

[7] P.J. Rosenfeld, D.M. Brown, J.S. Heier, D.S. Boyer, P.K. Kaiser, C.Y. Chung, et al., Ranibizumab for neovascular age-related macular degeneration, N. Engl. J. Med. 355 (14) (2006 Oct) 1419–1431.

[8] A. Uemura, M. Fruttiger, P.A. D'Amore, S. De Falco, A.M. Joussen, F. Sennlaub, et al., VEGFR1 signaling in retinal angiogenesis and microinflammation, Prog. Retin. Eye Res. 84 (2021 Sep) 100954.

[9] A.K. Olsson, A. Dimberg, J. Kreuger, L. Claesson-Welsh, VEGF receptor signaling - in control of vascular function, Nat. Rev. Mol. Cell Biol. 7 (5) (2006 May) 359–371.

[10] S. Selvam, T. Kumar, M. Fruttiger, Retinal vasculature development in health and disease, Prog. Retin. Eye Res. 63 (2018 Mar) 1–19.

[11] J.A. Wells, A.R. Glassman, A.R. Ayala, L.M. Jampol, N.M. Bressler, S.B. Bressler, et al., Aflibercept, Bevacizumab, or Ranibizumab for diabetic macular edema two-Year results from a Comparative Effectiveness randomized clinical trial, Ophthalmology 123 (6) (2016 Jun) 1351–1359.

[12] C. Krispel, M. Rodrigues, X. Xin, A. Sodhi, Ranibizumab in diabetic macular edema, World J. Diabetes 4 (6) (2013) 310–318.

[13] A.S. Tsai, H Da Chou, X.C. Ling, T. Al-Khaled, N. Valikodath, E. Cole, et al., Assessment and management of retinopathy of prematurity in the era of anti-vascular endothelial growth factor (VEGF), Prog. Retin. Eye Res. 88 (2022 May) 101018.

[14] K.G. Falavarjani, Q.D. Nguyen, Adverse events and complications associated with intravitreal injection of anti-VEGF agents: a review of literature, Eye (Basingstoke). 27 (7) (2013 Jul) 787–794.

[15] Z. Liu, J. Xu, Q. Ma, X. Zhang, Q. Yang, L. Wang, et al., Glycolysis links reciprocal activation of myeloid cells and endothelial cells in the retinal angiogenic niche, Sci. Transl. Med. 12 (555) (2020 Aug) eaay1371.

[16] K. Kataoka, K.M. Nishiguchi, H. Kaneko, N. Van Rooijen, S. Kachi, H. Terasaki, The roles of vitreal macrophages and circulating Leukocytes in retinal neovascularization, Investigative Ophthalmology & Visual Science 52 (3) (2011 Mar) 1431–1438.

[17] A. Fantin, J.M. Vieira, G. Gestri, L. Denti, Q. Schwarz, S. Prykhozhij, et al., Tissue macrophages act as cellular chaperones for vascular anastomosis downstream of VEGF-mediated endothelial tip cell induction, Blood 116 (5) (2010 Aug 5) 829–840.

[18] M. Locati, G. Curtale, A. Mantovani, Diversity, mechanisms, and significance of macrophage Plasticity, Annu. Rev. Pathol. 15 (2020 Jan) 123–147.

[19] K. Huang, Z. Lin, Y. Ge, X. Chen, Y. Pan, Z. Lv, et al., Immunomodulation of MiRNA-223-based nanoplatform for targeted therapy in retinopathy of prematurity, J. Contr. Release 350 (2022 Oct) 789–802.

[20] J. Li, S. Yu, X. Lu, K. Cui, X. Tang, Y. Xu, et al., The phase changes of M1/M2 phenotype of microglia/macrophage following oxygen-induced retinopathy in mice, Inflamm. Res. 70 (2) (2021 Feb 1) 183–192.

[21] X. Wang, C. Xu, C. Bian, P. Ge, J. Lei, J. Wang, et al., M2 microglia-derived exosomes promote vascular remodeling in diabetic retinopathy, J. Nanobiotechnol. 22 (1) (2024 Dec 1) 56.

[22] X. Ma, W. Wu, W. Liang, Y. Takahashi, J. Cai, J.X. Ma, Modulation of cGAS-STING signaling by PPARα in a mouse model of ischemia-induced retinopathy,

Proceedings of National Academy of Science the United States of America 119 (48) (2022 Nov) e2208934119.

[23] Y. Peng, J. Zhuang, G. Ying, H. Zeng, H. Zhou, Y. Cao, et al., Stimulator of IFN genes mediates neuroinflammatory injury by suppressing AMPK signal in experimental subarachnoid hemorrhage, J. Neuroinflammation 17 (1) (2020 May) 165.

[24] G.L. Jiang, X.L. Yang, H.J. Zhou, J. Long, B. Liu, L.M. Zhang, et al., cGAS knockdown promotes microglial M2 polarization to alleviate neuroinflammation by inhibiting cGAS-STING signaling pathway in cerebral ischemic stroke, Brain Res. Bull. 171 (2021 Jun) 183–195.

[25] Y.T. Wu, Y. Fang, Q. Wei, H. Shi, H. Tan, Y. Deng, et al., Tumor-targeted delivery of a STING agonist improves cancer immunotherapy, Proceedings of National Academy of Science the United States of America 119 (49) (2022 Dec) e2214278119.

[26] A. Decout, J.D. Katz, S. Venkatraman, A. Ablasser, The cGAS–STING pathway as a therapeutic target in inflammatory diseases, Nat. Rev. Immunol. 21 (9) (2021 Apr) 548–569.

[27] S.M. Haag, M.F. Gulen, L. Reymond, A. Gibelin, L. Abrami, A. Decout, et al., Targeting STING with covalent small-molecule inhibitors, Nature 559 (7713) (2018 Jul) 269–273.

[28] H. Shen, L. Jin, Q. Zheng, Z. Ye, L. Cheng, Y. Wu, et al., Synergistically targeting synovium STING pathway for rheumatoid arthritis treatment, Bioact. Mater. 24 (2023 Jun) 37–53.

[29] Z. Zhu, H. Lu, L. Jin, Y. Gao, Z. Qian, P. Lu, et al., C-176 loaded Ce DNase nanoparticles synergistically inhibit the cGAS-STING pathway for ischemic stroke treatment, Bioact. Mater. 29 (2023 Nov) 230–240.

[30] X. Huang, Y. Chau, Intravitreal nanoparticles for retinal delivery, Elsevier Ltd, Drug Discov. Today 24 (2019) 1510–1523.

[31] M. Okada, P. Mitchell, R.P. Finger, B. Eldem, S.J. Talks, C. Hirst, et al., Nonadherence or Nonpersistence to intravitreal injection therapy for neovascular age-related macular degeneration: a Mixed-Methods Systematic review, Ophthalmology 128 (2) (2021 Jan) 234–247.

[32] M. Okada, T.Y. Wong, P. Mitchell, B. Eldem, S.J. Talks, T. Aslam, et al., Defining Nonadherence and Nonpersistence to anti-vascular endothelial growth factor Therapies in neovascular age-related macular degeneration, JAMA Ophthalmology 139 (7) (2021 Jul) 769–776.

[33] W. Gao, Y. Liu, G. Jing, K. Li, Y. Zhao, B. Sha, et al., Rapid and efficient crossing blood-brain barrier: hydrophobic drug delivery system based on propionylated amylose helix nanoclusters, Biomaterials 113 (2017 Jan) 133–144.

[34] L. Zhang, X. Zhang, G. Lu, F. Li, W. Bao, C. Song, et al., Cell membrane Camouflaged hydrophobic drug Nanoflake Sandwiched with photosensitizer for orchestration of chemo-photothermal combination therapy, Small 15 (20) (2019 May) 1805544.

[35] P. Yang, S. Gai, J. Lin, Functionalized mesoporous silica materials for controlled drug delivery, Chem. Soc. Rev. 41 (9) (2012 Apr) 3679–3698.

[36] X. Deng, K. Chen, K. Pang, X. Liu, M. Gao, J. Ren, et al., Key progresses of MOE key laboratory of macromolecular synthesis and functionalization in 2022, Chin. Chem. Lett. 35 (3) (2024 Mar) 108861.

[37] D. Shen, J. Yang, X. Li, L. Zhou, R. Zhang, W. Li, et al., Biphase stratification approach to three-dimensional dendritic biodegradable mesoporous silica nanospheres, Nano Lett. 14 (2) (2014 Feb) 923–932.

[38] A. Kienzle, S. Kurch, J. Schlöder, C. Berges, R. Ose, J. Schupp, et al., Dendritic mesoporous silica nanoparticles for pH-stimuli-responsive drug delivery of TNF-alpha, Adv. Healthcare Mater. 6 (13) (2017 Jul) 1700012.

[39] Y. Feng, Z. Liao, M. Li, H. Zhang, T. Li, X. Qin, et al., Mesoporous silica nanoparticles-based nanoplatforms: basic construction, current state, and emerging applications in anticancer therapeutics, Adv. Healthcare Mater. 12 (16) (2023 Jun).

[40] X. Li, Y. Liu, X. Qi, S. Xiao, Z. Xu, Z. Yuan, et al., Sensitive activatable nanoprobes for real-time ratiometric magnetic resonance imaging of reactive oxygen species and ameliorating inflammation in vivo, Adv. Mater. 34 (19) (2022 May) 2109004.

[41] N. Scott-Hewitt, F. Perrucci, R. Morini, M. Erreni, A. Mahoney, A. Witkowska, et al., Local externalization of phosphatidylserine mediates developmental synaptic pruning by microglia, EMBO J. 39 (16) (2020 Aug 17) e105380.

[42] Y. Liu, W.N. Crowe, L. Wang, Y. Lu, W.J. Petty, A.A. Habib, et al., An inhalable nanoparticulate STING agonist synergizes with radiotherapy to confer long-term control of lung metastases, Nat. Commun. 10 (1) (2019 Dec 1) 5108.

[43] L. Li, J. Zou, Y. Dai, W. Fan, G. Niu, Z. Yang, et al., Burst release of encapsulated annexin A5 in tumours boosts cytotoxic T-cell responses by blocking the phagocytosis of apoptotic cells, Nat. Biomed. Eng. 4 (11) (2020 Nov) 1102–1116.

[44] M. Tredicine, F. Ria, N. Poerio, M. Lucchini, A. Bianco, F. De Santis, et al., Liposome-based nanoparticles impact on regulatory and effector phenotypes of macrophages and T cells in multiple Sclerosis patients, Biomaterials 292 (2023 Jan) 121930.

[45] D. Shen, J. Yang, X. Li, L. Zhou, R. Zhang, W. Li, et al., Biphase stratification approach to three-dimensional dendritic biodegradable mesoporous silica nanospheres, Nano Lett. 14 (2) (2014 Feb) 923–932.

[46] H. Yang, Y. Ding, Z. Tong, X. Qian, H. Xu, F. Lin, et al., pH-responsive hybrid platelet membrane-coated nanobomb with deep tumor penetration ability and enhanced cancer thermal/chemodynamic therapy, Theranostics 12 (9) (2022) 4250–4268.

[47] K.M. Connor, N.M. Krah, R.J. Dennison, C.M. Aderman, J. Chen, K.I. Guerin, et al., Quantification of oxygen-induced retinopathy in the mouse: a model of vessel loss, vessel regrowth and pathological angiogenesis, Nat. Protoc. 4 (11) (2009) 1565–1573.

[48] J. Wang, E. Du, F.F. Li, Y. Zheng, Changes of Beclin-1 and ULK1 in retina of mice model in oxygen-induced retinopathy, Advances in Ophthalmology Practice and Research 2 (3) (2022 Nov 1) 100065.

[49] Z. Liu, S. Yan, J. Wang, Y. Xu, Y. Wang, S. Zhang, et al., Endothelial adenosine A2a receptor-mediated glycolysis is essential for pathological retinal angiogenesis, Nat. Commun. 8 (1) (2017 Dec) 584.

[50] Y. Murakami, K. Ishikawa, S. Nakao, K.H. Sonoda, Innate immune response in retinal homeostasis and inflammatory disorders, Prog. Retin. Eye Res. 74 (2020 Jan) 100778.

[51] P.G. McMenamin, D.R. Saban, S.J. Dando, Immune cells in the retina and choroid: two different tissue environments that require different defenses and surveillance, Prog. Retin. Eye Res. 70 (2019 May) 85–98.

[52] S.Y. Choi, J.Y. Choi, J.M. Lee, S. Lee, E.J. Cho, Tartary buckwheat on nitric oxide-induced inflammation in RAW264.7 macrophage cells, Food Funct. 6 (8) (2015 Aug) 2664–2670.

[53] J.W. Hartley, L.H. Evans, K.Y. Green, Z. Naghashfar, A.R. Macias, P.M. Zerfas, et al., Expression of infectious murine leukemia viruses by RAW264.7 cells, a potential complication for studies with a widely used mouse macrophage cell line, Retrovirology 5 (2008 Jan).

[54] H. Wu, H. Dong, Z. Tang, Y. Chen, Y. Liu, M. Wang, et al., Electrical stimulation of piezoelectric BaTiO3 coated Ti6Al4V scaffolds promotes anti-inflammatory polarization of macrophages and bone repair via MAPK/JNK inhibition and OXPHOS activation, Biomaterials 293 (2023 Feb) 121990.

[55] P.S. Mettu, M.J. Allingham, S.W. Cousins, Incomplete response to Anti-VEGF therapy in neovascular AMD: exploring disease mechanisms and therapeutic opportunities, Prog. Retin. Eye Res. 82 (2021 May) 100906.

[56] A. Hellström, L.E.H. Smith, O. Dammann, Retinopathy of prematurity, Lancet 382 (2013 Oct) 1445–1457.

[57] Y. Zhou, S. Yoshida, S. Nakao, T. Yoshimura, Y. Kobayashi, T. Nakama, et al., M2 macrophages enhance pathological neovascularization in the mouse model of oxygen-induced retinopathy, Investigative Ophthalmology & Visual Science 56 (8) (2015 Jul 1) 4767–4777.

[58] X. Chen, X. Wang, Z. Cui, Q. Luo, Z. Jiang, Y. Huang, et al., M1 microglia-derived exosomes promote activation of resting microglia and amplifies proangiogenic effects through irf1/miR-155-5p/socs1 Axis in the retina, International Journal of Biological Science 19 (6) (2023) 1791–1812.

[59] X. Chen, X. Wang, Z. Cui, Q. Luo, Z. Jiang, Y. Huang, et al., M1 microglia-derived exosomes promote activation of resting microglia and amplifies proangiogenic effects through irf1/miR-155-5p/socs1 Axis in the retina, International Journal of Biological Science 19 (6) (2023) 1791–1812.

[60] W. Xia, C. Li, Q. Chen, J. Huang, Z. Zhao, P. Liu, et al., Intravenous route to choroidal neovascularization by macrophage-disguised nanocarriers for mTOR modulation, Acta Pharm. Sin. B 12 (5) (2022 May 1) 2506–2521.

[61] D.D. Nguyen, L.J. Luo, C.J. Yang, J.Y. Lai, Highly retina-permeating and long-acting resveratrol/metformin nanotherapeutics for enhanced treatment of macular degeneration, ACS Nano 17 (1) (2023 Jan 10) 168–183.

[62] M. Bohley, A.E. Dillinger, F. Schweda, A. Ohlmann, B.M. Braunger, E.R. Tamm, et al., A single intravenous injection of cyclosporin A-loaded lipid nanocapsules prevents retinopathy of prematurity, Sci. Adv. 8 (38) (2022 Sep) eabo6638.

[63] M. Li, Z. Xu, L. Zhang, M. Cui, M. Zhu, Y. Guo, et al., Targeted noninvasive treatment of choroidal neovascularization by hybrid cell-membrane-cloaked biomimetic nanoparticles, ACS Nano 15 (6) (2021 Jun 22) 9808–199.

[64] Y. Zhou, M. Xu, W. Shen, Y. Xu, A. Shao, P. Xu, et al., Recent advances in nanomedicine for ocular fundus neovascularization disease management (early access), Adv. Healthcare Mater. (2024 Mar).

[65] M. Vallet-Regí, F. Schüth, D. Lozano, M. Colilla, M. Manzano, Engineering mesoporous silica nanoparticles for drug delivery: where are we after two decades? Chem. Soc. Rev. 51 (13) (2022 Jul 4) 5365–5451.

[66] E. Phillips, O. Penate-Medina, P.B. Zanzonico, R.D. Carvajal, P. Mohan, Y. Ye, et al., Clinical translation of an ultrasmall inorganic optical-PET imaging nanoparticle probe, Sci. Transl. Med. 6 (260) (2014 OCT 29) 260ra149.